

Unsteady Aerodynamic and Aeroelastic Calculations for Wings Using Euler Equations

Guru P. Guruswamy*

NASA Ames Research Center, Moffett Field, California

A procedure to solve simultaneously the Euler flow equations and modal structural equations of motion is presented for computing aeroelastic responses of wings. The Euler flow equations are solved by a finite-difference scheme with dynamic grids. The coupled aeroelastic equations of motion are solved using the linear-acceleration method. The aeroelastic configuration adaptive dynamic grids are time-accurately generated using the aeroelastically deformed shape of the wing. The unsteady flow calculations are validated with the experiment, both for a semi-infinite wing and a wall-mounted cantilever rectangular wing. Aeroelastic responses are computed for a rectangular wing using the modal data generated by the finite-element method. The robustness of the present approach in computing unsteady flows and aeroelastic responses that are beyond the capability of earlier approaches using potential equations are demonstrated.

Introduction

IN the last two decades, there have been extensive developments in computational aerodynamics that constitute a major part of the general area of computational fluid dynamics (CFD).^{1,2} Such developments are essential to advance the understanding of the physics of complex flows, complement expensive wind-tunnel tests, and reduce the overall design cost of an aircraft. The CFD capabilities have advanced closely in phase with the improvements in computer resources. In general, computational aerodynamics can be classified based on the type of equations used and complexity of the configuration considered. The problem can be further grouped into those involving steady and unsteady flows.

Computational methods to analyze wing problems involving steady flows have advanced to the level of using the Navier-Stokes equations, and calculations on wing-body configurations are in progress.³ In comparison, for unsteady flows associated with moving components such as oscillating wings, the most advanced codes use methods based on the potential-flow theory.⁴ Some of the reasons for the lag in the development of unsteady methods when compared to steady methods are 1) the complexity of physics associated with the movement of flexible components, 2) the complexity in modeling the flow because of the moving grids, and 3) the lack of development of fast, time-accurate methods. One of the main reasons to develop efficient unsteady methods is to understand the interaction of the flows with moving structural components such as the aeroelasticity of an aircraft.

Aeroelasticity plays an important role in the design and development of an aircraft, particularly modern aircraft, which tend to be flexible for high maneuverability. Several phenomena that can be dangerous and limit the performance of an aircraft occur because of the interaction of the flow with

flexible components. For example, aircraft with highly swept wings experience vortex-induced aeroelastic oscillations.^{5,6} Also, several undesirable aeroelastic phenomena occur in the transonic range that are due to the presence and movement of shock waves. Limited wind-tunnel and flight tests have shown aeroelastically critical phenomena such as a low transonic flutter speed. Because of the high cost and risk involved, it is not practical to conduct extensive aeroelastic tests. An aeroelastic wind-tunnel experiment is an order of magnitude more expensive than a parallel experiment involving only aerodynamics. By complementing the wind-tunnel experiments with the computational techniques, the overall cost of the development of an aircraft can be considerably reduced.

At present, the most advanced codes used for aeroelastic analyses, such as XTRAN3S,⁷ use the transonic small-perturbation equation. Currently, ATRAN3S, the NASA-Ames version of XTRAN3S, is being used for generic research in unsteady aerodynamics and aeroelasticity of full-span, wing-body configurations.⁴ Although codes based on the potential-flow theory give some useful results, they cannot be used for cases involving complex flows. Now, given the availability of new efficient numerical techniques and faster computers,⁸ it is time to consider Euler/Navier-Stokes equations for aeroelastic applications.

Codes based on the Euler/Navier-Stokes equations have already been applied for practical and interesting problems involving steady flows. Generic codes, such as ARC3D,⁹ NASA Ames Research Center's three-dimensional Euler/Navier-Stokes code, have been used for several scientific investigations. Such generic codes have resulted in useful codes such as TNS, NASA-Ames's Transonic Navier-Stokes code based on zonal grids. TNS has successfully computed complex separated flows on wings and wing-body configurations.³

In this paper, a computational method for computing unsteady flows and aeroelastic responses of flexible wings is presented. This work is a part of a larger effort within the Applied Computational Fluids Branch of NASA Ames Research Center to develop a new code, ENSAERO, an efficient general-purpose code to compute unsteady aerodynamics and aeroelasticity of aircraft using the Euler/Navier-Stokes equations. This new code is being designed in a modular fashion to adapt several different numerical schemes suitable for accurate aeroelastic computations. The candidate flow solvers are based on schemes such as central-difference schemes with artificial viscosity,¹⁰ upwind schemes,^{11,12} etc., which have mostly

Presented as Paper 88-2281 at the AIAA/ASME/ASCE/AHS 29th Structures, Structural Dynamics, and Materials Conference, Williamsburg, VA, April 18-20, 1988; received May 10, 1988; revision received Jan. 6, 1989. Copyright © 1989 American Institute of Aeronautics and Astronautics, Inc. No copyright is asserted in the United States under Title 17, U.S. Code. The U.S. Government has a royalty-free license to exercise all rights under the copyright claimed herein for Governmental purposes. All other rights are reserved by the copyright owner.

*Research Scientist, Applied Computational Fluids Branch. Associate Fellow AIAA.

been applied for steady flows and, in some cases, for unsteady flows over stationary bodies. The basic coding of ENSAERO can accommodate zonal grid techniques for efficient modeling of full aircraft.³ ENSAERO is also being designed in such a way that instead of the modal equations of motion, finite elements can be directly used for more complete modeling of structures.

This paper describes the first version, ENSAERO version 1.0, which is based on the Euler equations coupled with the modal structural equations of motion. Although computations in this paper are done using the Euler equations coupled with the modal structural equations of motion, all techniques developed in this work can be easily extended for computations using the Navier-Stokes equations directly coupled with the structural equations based on the finite-element method. The procedure to solve the flow equations in ENSAERO version 1.0 is based on the diagonal algorithm form¹³ of the Beam-Warming central-difference scheme.¹⁰ For the first time, this finite-difference scheme is adopted for aeroelastic computations using configuration adaptive dynamic grids. The coupled flow and modal structural equations of motion are solved using a simultaneous-integration technique based on the linear-acceleration technique. Dynamic grids that are adaptive to the deforming shapes of the wing are generated using an algebraic grid-generation scheme. The unsteady flow computations are validated with the experimental data for both a semi-infinite wing oscillating in pitching mode, and a wall-mounted cantilever finite wing oscillating in the first bending mode. The aeroelastic responses are computed for a rectangular wing using the modal data generated by the finite-element method and they are correlated with the experiment. The robustness of the present approach in computing aeroelastic responses that are beyond the capability of earlier approaches using potential flow equations is demonstrated.

Governing Aerodynamics Equations and Approximations

The strong conservation law form of the Euler equations is used for shock-capturing purposes. The equations in Cartesian coordinates in nondimensional form¹⁴ can be written as

$$\frac{\partial Q}{\partial t} + \frac{\partial E}{\partial x} + \frac{\partial F}{\partial y} + \frac{\partial G}{\partial z} = 0 \quad (1)$$

where

$$Q = \begin{bmatrix} \rho \\ \rho u \\ \rho v \\ \rho w \\ e \end{bmatrix}, \quad E = \begin{bmatrix} \rho u \\ \rho u^2 + p \\ \rho uv \\ \rho uw \\ (e+p)u \end{bmatrix}, \quad F = \begin{bmatrix} \rho v \\ \rho uv \\ \rho v^2 + p \\ \rho vw \\ (e+p)v \end{bmatrix}$$

$$G = \begin{bmatrix} \rho w \\ \rho uw \\ \rho vw \\ \rho w^2 + p \\ (e+p)w \end{bmatrix} \quad (2)$$

The Cartesian velocity components u , v , and w are nondimensionalized by a_∞ (the freestream speed of sound); density ρ is nondimensionalized by ρ_∞ ; the total energy per unit volume e is nondimensionalized by $\rho_\infty a_\infty^2$, and the time t is nondimensionalized by c/a , where c is the root chord. Pressure can be found from the ideal gas law as

$$p = (\gamma - 1)[e - 0.5\rho(u^2 + v^2 + w^2)] \quad (3)$$

and throughout γ is the ratio of the specific heats.

To enhance numerical accuracy and efficiency and to handle boundary conditions more easily, the governing equations are transformed from the Cartesian coordinates to general curvilinear coordinates using

$$\begin{aligned} \tau &= t \\ \xi &= \xi(x, y, z, t) \\ \eta &= \eta(x, y, z, t) \\ \zeta &= \zeta(x, y, z, t) \end{aligned} \quad (4)$$

The resulting transformed equations can be written in non-dimensional form as

$$\frac{\partial \hat{Q}}{\partial \tau} + \frac{\partial \hat{E}}{\partial \xi} + \frac{\partial \hat{F}}{\partial \eta} + \frac{\partial \hat{G}}{\partial \zeta} = 0 \quad (5)$$

where $\hat{\cdot}$ indicate the transformed quantities, and where

$$\hat{Q} = J^{-1} \begin{bmatrix} \rho \\ \rho u \\ \rho v \\ \rho w \\ e \end{bmatrix}, \quad \hat{E} = J^{-1} \begin{bmatrix} \rho U \\ \rho u U + \xi_x p \\ \rho v U + \xi_y p \\ \rho w U + \xi_z p \\ (e+p)U - \xi_i p \end{bmatrix}$$

$$\hat{F} = J^{-1} \begin{bmatrix} \rho V \\ \rho u V + \eta_x p \\ \rho v V + \eta_y p \\ \rho w V + \eta_z p \\ (e+p)V - \eta_i p \end{bmatrix}, \quad \hat{G} = J^{-1} \begin{bmatrix} \rho W \\ \rho u W + \zeta_x p \\ \rho v W + \zeta_y p \\ \rho w W + \zeta_z p \\ (e+p)W - \zeta_i p \end{bmatrix} \quad (6)$$

and

$$U = \xi_t + \xi_x u + \xi_y v + \xi_z w \quad (7a)$$

$$V = \eta_t + \eta_x u + \eta_y v + \eta_z w \quad (7b)$$

$$W = \zeta_t + \zeta_x u + \zeta_y v + \zeta_z w \quad (7c)$$

In Eqs. (7), U , V , and W are contravariant velocity components written without metric normalization. Here, the Cartesian derivatives are expanded in ξ , η , ζ space via chain-rule relations such as

$$u_x = \xi_x u_\xi + \eta_x u_\eta + \zeta_x u_\zeta \quad (8)$$

Finally, the metric terms are obtained from chain-rule expansion of x_ξ , y_η , etc., and solved for ξ_x , ξ_y , etc., to give

$$\xi_x = J(y_\eta z_\zeta - y_\zeta z_\eta), \quad \eta_x = J(z_\xi y_\zeta - y_\xi z_\zeta) \quad (9a)$$

$$\xi_y = J(z_\eta x_\zeta - x_\eta z_\zeta), \quad \eta_y = J(x_\xi z_\zeta - x_\zeta z_\xi) \quad (9b)$$

$$\xi_z = J(x_\eta y_\zeta - y_\eta x_\zeta), \quad \eta_z = J(y_\xi x_\zeta - x_\xi y_\zeta) \quad (9c)$$

$$\xi_x = J(y_\xi z_\eta - z_\xi y_\eta), \quad \xi_t = -x_\tau \xi_x - y_\tau \xi_y - z_\tau \xi_z \quad (9d)$$

$$\xi_y = J(x_\eta z_\xi - x_\xi z_\eta), \quad \eta_t = -x_\tau \eta_x - y_\tau \eta_y - z_\tau \eta_z \quad (9e)$$

$$\xi_z = J(x_\xi y_\eta - y_\xi x_\eta), \quad \zeta_t = -x_\tau \zeta_x - y_\tau \zeta_y - z_\tau \zeta_z \quad (9f)$$

and

$$J^{-1} = x_\xi y_\eta z_\zeta + x_\zeta y_\xi z_\eta + x_\eta y_\zeta z_\xi - x_\xi y_\zeta z_\eta - x_\eta y_\xi z_\zeta - x_\zeta y_\eta z_\xi \quad (10)$$

Several numerical schemes have been developed to solve Eq. (5). In this work, the algorithm developed by Beam and Warm-

ing¹⁰ and the diagonal algorithm extension reported by Pulliam and Chaussee,¹³ both based on implicit approximate factorization, are used. Both algorithms were implemented in a new code, ENSAERO, a general-purpose aeroelastic code based on the Euler/Navier-Stokes equations and the modal structural equations of motion with time-accurate aeroelastic configuration adaptive grids. (Results presented in this paper are from ENSAERO version 1.0, which uses the diagonal algorithm to solve the Euler equations.)

The diagonal algorithm used in this paper is a simplified version of the Beam-Warming scheme. In the diagonal algorithm, the flux Jacobians are diagonalized so that the computational operation count is reduced by 50%. The diagonal scheme is first-order accurate in time and yields time-accurate shock calculations in a nonconservative mode. The scheme used is briefly explained in the Appendix. More details of this scheme can be found in Ref. 13.

Aeroelastic Equations of Motion

The governing aeroelastic equations of motion of a flexible wing are solved by using the Rayleigh-Ritz method. In this method, the resulting aeroelastic displacements at any time are expressed as a function of a finite set of assumed modes. The contribution of each assumed mode to the total motion is derived by Lagrange's equation. Furthermore, it is assumed that the deformation of the continuous wing structure can be represented by deflections at a set of discrete points. This assumption facilitates the use of discrete structural data, such as the modal vector, the modal stiffness matrix, and the modal mass matrix. These can be generated from a finite-element analysis or from experimental influence coefficient measurements. In this study, the finite-element method is employed to obtain the modal data.

It is assumed that the deformed shape of the wing can be represented by a set of discrete displacements at selected nodes. From the modal analysis, the displacement vector $\{d\}$ can be expressed as

$$\{d\} = [\psi]\{q\} \quad (11)$$

where $[\psi]$ is the modal matrix and $\{q\}$ is the generalized displacement vector. The final matrix form of the aeroelastic equations of motion is

$$[M]\{\ddot{q}\} + [G]\{\dot{q}\} + [K]\{q\} = \{F\} \quad (12)$$

where $[M]$, $[G]$, and $[K]$ are modal mass, damping, and stiffness matrices, respectively. The $\{F\}$ is the aerodynamic force vector defined as $(\frac{1}{2})\rho U_\infty^2 [\psi]^T [A] \{\Delta C_p\}$ and $[A]$ is the diagonal area matrix of the aerodynamic control points.

The aeroelastic equation of motion (12) is solved by a numerical integration technique based on the linear-acceleration method.¹⁵ Assuming a linear variation of the acceleration, the velocities and displacements at the end of a time interval t can be derived as follows:

$$\{\dot{q}\}_t = \{\dot{q}\}_{t-\Delta t} + \left(\frac{\Delta t}{2}\right)\{\ddot{q}\}_{t-\Delta t} + \left(\frac{\Delta t}{2}\right)\{\ddot{q}\}_t \quad (13a)$$

$$\begin{aligned} \{q\}_t &= \{q\}_{t-\Delta t} + (\Delta t)\{\dot{q}\}_{t-\Delta t} + \left(\frac{\Delta t^2}{3}\right)\{\ddot{q}\}_{t-\Delta t} \\ &+ \left(\frac{\Delta t^2}{6}\right)\{\ddot{q}\}_t \end{aligned} \quad (13b)$$

$$\{\ddot{q}\}_t = [D]\left(\{F\}_t - [G]\{v\} - [K]\{w\}\right) \quad (13c)$$

where

$$[D] = \left([M] + \frac{\Delta t}{2}[G] + \frac{\Delta t^2}{6}[K]\right)^{-1}$$

$$v = \{\dot{q}\}_{t-\Delta t} + \left(\frac{\Delta t}{2}\right)\{\ddot{q}\}_{t-\Delta t}$$

$$w = \{q\}_{t-\Delta t} + (\Delta t)\{\dot{q}\}_{t-\Delta t} + \left(\frac{\Delta t^2}{3}\right)\{\ddot{q}\}_{t-\Delta t}$$

These equations can also be derived by using the second-order-accurate central-difference scheme. Since Eqs. (13) are explicit in time, the computational time-step size is restricted by stability considerations. However, the time-step size required to solve the aerodynamic equation [Eq. (5)] accurately is always far less than the time-step size required to obtain stable and accurate solution using the preceding numerical-integration scheme.¹⁵ To obtain physically meaningful time-accurate solutions, it is necessary to use the same time-step size in integrating Eq. (5) and Eq. (12). Also, the preceding scheme is numerically nondissipative and does not lead to any nonphysical aeroelastic phenomenon.

The step-by-step integration procedure for obtaining the aeroelastic response was performed as follows. Assuming that freestream conditions and wing-surface boundary conditions were obtained from a set of selected starting values of the generalized displacement, velocity, and acceleration vectors, the generalized aerodynamic force vector $\{F(t)\}$ at time t was computed by solving Eq. (5). Using this aerodynamic vector, the generalized displacement, velocity, and acceleration vectors for the time level t are calculated by Eq. (12). From the generalized coordinates computed at the time level t , the new boundary conditions on the surface of the wing are computed. With these new boundary conditions, the aerodynamic vector $\{F(t)\}$ at the next time level, $t + \Delta t$, is computed using Eq. (5). This process is repeated every time step to advance the aerodynamic and structural equations of motion forward in time until the required response is obtained.

Aeroelastic Configuration Adaptive Grids

One of the major complexities in computational aerodynamics using the Euler equations lies in the area of grid generation. For the case of steady flows, advanced techniques such as zonal grids³ are currently being used. Grid-generation techniques for aeroelastic calculations that involve moving components are in an early stage of development. The effects of the aeroelastic configuration adaptive dynamic grids on the stability and accuracy of the numerical schemes are yet to be studied in detail.

This work developed an analytical grid-generation technique for aeroelastic applications. This scheme satisfies the general requirements of a grid required for implicit finite-difference schemes used in the present analysis.^{10,13} Some of the requirements are 1) grid lines intersect normal to the wing surface in the chordwise direction, 2) a smooth stretching of grid cells away from the wing surface, 3) outer boundaries located far away from the wing to minimize the effect of boundary reflections, and 4) a grid that adapts to the deformed wing position at each time step. The type of grid used is C-H grid. The grid is generated at every time step based on the aeroelastic position of the wing computed using Eq. (12) as follows.

At the end of every time step, the deformed shape of the wing is computed using Eq. (11). The ξ and η grid distributions on the grid surface corresponding to the wing surface (ζ grid index = 1) are obtained from previously assumed distributions. These distributions are selected to satisfy the general requirements of a grid for accurate computations. In this work, the grid in the ξ direction is selected such that the grid spacing is fine on the wing and it stretches exponentially to outer boundaries. The grid near the nose is finer than the rest

of the wing in order to model the nose geometry accurately. In the spanwise direction, a uniformly distributed grid spacing is used on the wing. In order to model the wing tip, a finer grid spacing is used near the wing tip. Away from the wing tip, the η grid spacing stretches exponentially. The ζ grid spacing is computed every time step using the deformed shape of the wing computed by using Eq. (11). The ζ grid lines start normal to the surface in the chordwise directions and their spacing stretches exponentially to a fixed outer boundary. In order to restrain the outer boundaries from moving, the grid is sheared in the ζ direction. The metrics required in the computational domain are computed using the following relations:

$$\xi_t = -x_\tau \xi_x - y_\tau \xi_y - z_\tau \xi_z \quad (14a)$$

$$\eta_t = -x_\tau \eta_x - y_\tau \eta_y - z_\tau \eta_z \quad (14b)$$

$$\zeta_t = -x_\tau \zeta_x - y_\tau \zeta_y - z_\tau \zeta_z \quad (14c)$$

The grid velocities x_τ , y_τ , and z_τ required in Eqs. (14) are computed using the grids at new and old time levels. This configuration adaptive grid-generation scheme is incorporated in ENSAERO. Figures 1a and 1b show grids around a wing section in a x - z plane at 50% span for two positions of a rectangular wing. Similarly, Fig. 2a and 2b show grids in a x - z plane at the 50% chord axis for two positions of a rectangular wing in bending motion. Both Figs. 1 and 2 show the ability of the grid to conform to the deforming wing surface.

Results

Aerodynamic Computations for a Semi-infinite Wing

In this section, steady and unsteady computations are made to validate the accuracy and to demonstrate the capability of

the present flow computations. The unsteady results shown are from the computations made for wings undergoing prescribed forced motions.

Time accuracy is an essential requirement for aeroelastic computations. Numerical schemes used for flow calculations in aeroelasticity must guarantee the correct calculation of amplitude and phase of unsteady pressures. In order to verify the time accuracy of the flow calculations, a semi-infinite wing with an NACA 64A010 airfoil section was selected. This case was selected to assess the accuracy of the computed results against the available two-dimensional experimental data.¹⁶

For the semi-infinite rectangular wing configuration considered, a C-H type grid with 110 points in the chordwise direction, 20 points in the spanwise direction, and 20 points in the normal direction, was used. Using this dynamic grid which adapts according to the airfoil position as shown in Fig. 1, several unsteady calculations were made for the semi-infinite wing. All computations were made at a transonic Mach number of 0.8 for a reduced frequency of 0.1 (based on the full chord) when the wing was oscillating sinusoidally in pitch mode with an amplitude of 1.03 deg about a mean angle of attack of -0.21 deg.

In order to study the accuracy and stability of the scheme, inviscid computations using the Euler equation [Eq. (5)] were made with 720, 1080, and 1440 time steps/cycle. The computations were started with freestream flow conditions as initial data, and continued for three cycles of wing oscillation to obtain a periodic solution. A Fourier analysis was carried out on the third cycle of the solution to obtain real and imaginary

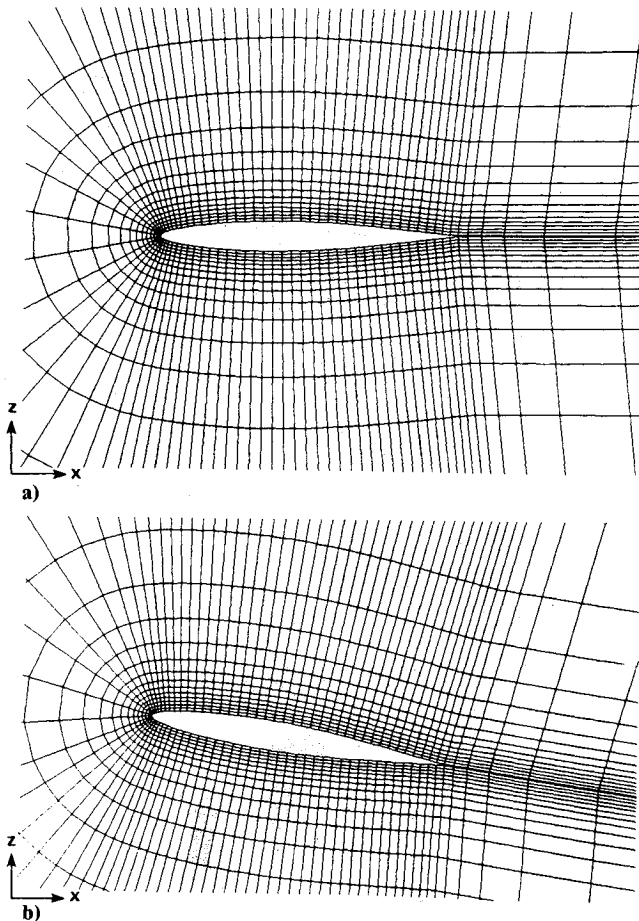


Fig. 1 Chordwise view of grid in x - z plane at 50% semispan location: a) initial position, and b) deformed position.

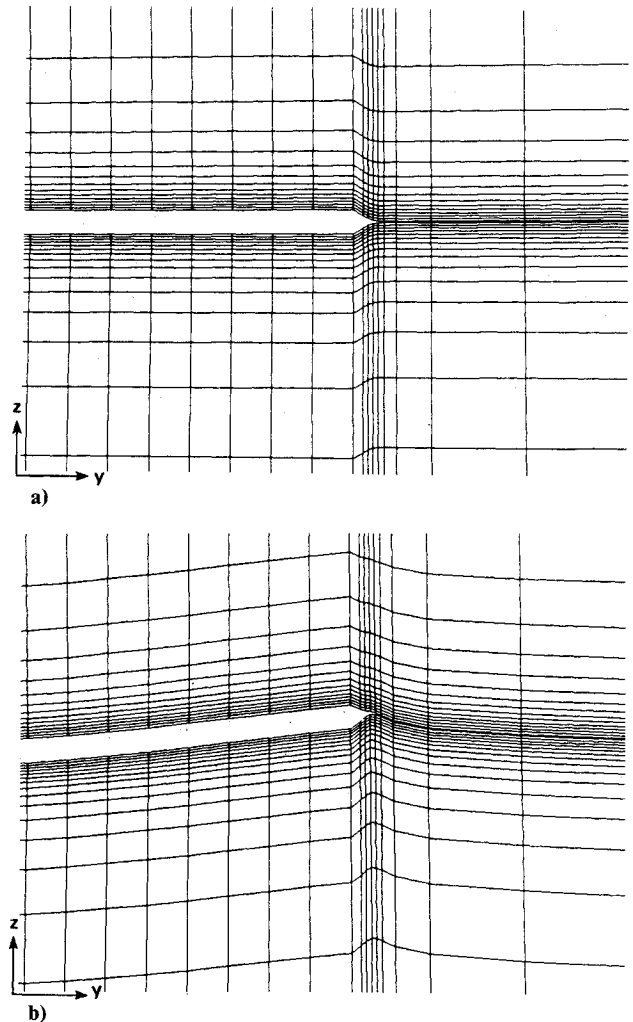


Fig. 2 Spanwise view of grid in y - z plane at 50% chord location: a) initial position, and b) deformed position.

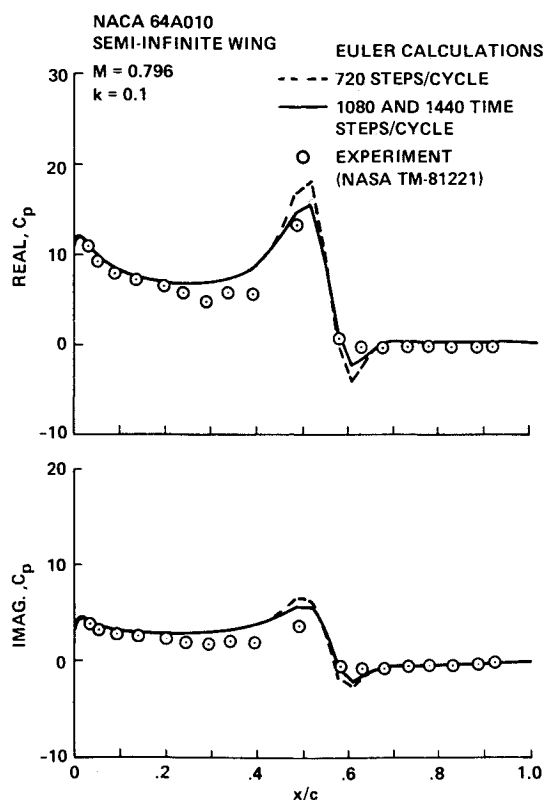


Fig. 3 Real and imaginary components of unsteady lower surface pressures at midspan of the semi-infinite wing.

parts of unsteady harmonic pressure history and these are shown in Fig. 3 for the three computational time-step sizes considered. Also shown in Fig. 3 are the experimental measurements of Ref. 16. The results obtained using 1080 and 1440 time steps/cycle are essentially identical, and they differ slightly from the result obtained using 720 time steps/cycle. It is also noted that the Fourier results from the second cycle were identical to those from the third cycle. From these observations, it can be stated that the present scheme required three cycles of oscillations with 1080 time steps/cycle, during which time the unsteady transients disappeared and a periodic response was obtained. Good comparisons with the experiment illustrates that the present procedure of solving Eq. (5) using a dynamic grid gives accurate results.

In Fig. 4, the results from the Euler calculations are compared with those from ATRAN2,¹⁷ a two-dimensional unsteady code based on the classical transonic small-perturbation theory. The Euler results compare better with the experiment than the results from ATRAN2. This illustrates the inadequacy of the potential flow theory for a moderately thick NACA 64A010 airfoil even at a small angle of attack of -0.21° . This inadequacy of the potential flow theory is because of the lack of accurate modeling of entropy and vorticity. In order to illustrate the capability of the Euler equations further, unsteady calculations were made at 4.0° mean angle of attack and the results are shown in Fig. 5. It is noted that these results cannot be computed using the classical potential flow equations because of numerical instability caused by a strong shock wave that lies close to the trailing edge.

Aerodynamic Computations for a Rectangular Wing

In order to validate the present computations for a finite wing undergoing a prescribed forced motion, a rectangular wing of aspect ratio 3 with a 5% thick circular arc section was selected. For this wing, steady and unsteady experimental data are given in Ref. 18. The unsteady pressures were measured when the wing was undergoing a forced sinusoidal motion in

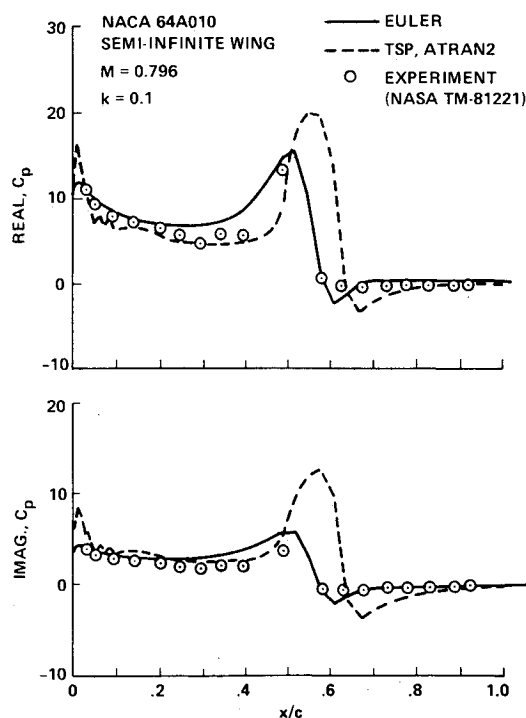


Fig. 4 Comparison of unsteady pressures between Euler and potential flow calculations.

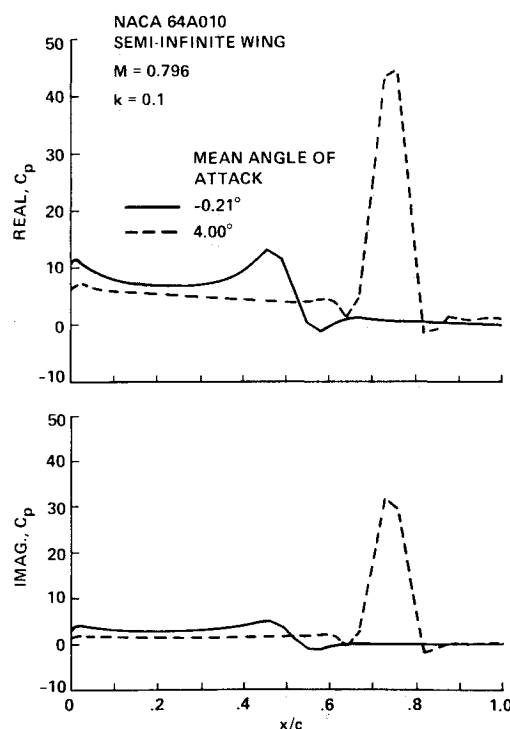


Fig. 5 Comparison of unsteady pressures between small and medium angles of attack from Euler flow calculations.

its first bending mode. The measured modal data from Ref. 18 were used in the present computations. All computations were made with a grid of size $110 \times 20 \times 20$.

Figure 6 shows computed and experimental steady pressure distributions at four spanwise stations for subsonic flow ($M = 0.70$ and $\alpha = 5.0^\circ$). Similarly, Fig. 7 shows computed and experimental steady pressure distributions at four span stations for transonic flow ($M = 0.90$ and $\alpha = 0.0^\circ$). For both cases, upper and lower surface results compare well with

the experiment. The discrepancies seen near the nose for the subsonic case in Fig. 6 are because of the lack of grid resolution near the nose. A grid finer than the one used in this analysis is required to improve the computed results. The discrepancies seen at the root span station in Fig. 7 for the transonic flow are because of viscous effects from the wall which cannot be modeled with the Euler equations used in the present analysis. An accurate modeling of viscous effects requires the use of the Navier-Stokes equation.

The unsteady aerodynamic pressures were computed by forcing the wing to undergo a sinusoidal modal motion and integrating the aerodynamic equation of motion in time. The modal motion simulated in the code was the first bending mode that was used in the experiment. For all of the cases studied here, it was found that about three cycles of motion with 1440 time steps/cycle were sufficient to obtain a periodic aerodynamic response. Periodicity was tested by comparing the responses between the second and third cycles. The magnitudes and phase angles of the unsteady differential pressure coefficients ($\Delta C_p = C_{pl} - C_{pu}$) were computed using the third cycle results.

In Fig. 8, the magnitudes and phase angles of the unsteady differential pressures obtained by ENSAERO and the experiment are shown for four spanwise stations for $M = 0.70$ and $k = 0.34$. In the same figure, results obtained by the kernel function method¹⁸ are also shown. The phase-angle results from the experiment are not shown since those results at this Mach number were corrupted by the wind-tunnel resonance as reported in Ref. 18. In general, the three sets of curves agree well. The agreement of the magnitudes is better than that of

phase angles. These unsteady computations illustrate the accuracy of the present computations using a dynamic grid for a finite wing.

In Fig. 9, the magnitudes and phase angles of the unsteady differential pressures obtained by ENSAERO and the experiment are shown for four span stations for transonic flow ($M = 0.90$ and $k = 0.26$). In general, the two sets of results compare fairly well except near the root. Peaks in pressure differences occur at almost the same locations for both ENSAERO and the experiment. The computed results show the characteristic jump in the transonic phase angle behind the shock wave shown by several experiments. Correct prediction of this characteristic verifies the time accuracy of the present computations. The computed pressure differences near the shock are more pronounced than the measured data. This discrepancy may be attributed to the viscous effects that are not accounted for in the Euler equations. These discrepancies are magnified near the root because of the additional effect of the wall boundary layer. The computed results show some oscillations, particularly in the phase near the root. Numerical experiments performed during the present study revealed that these oscillations can be suppressed by using finer grid spacings.

Aeroelastic Computations for a Rectangular Wing

This section shows aeroelastic results computed from the coupled flow and structural equations of motion, Eq. (12). Aeroelastic-response analyses are conducted for a uniform rectangular wing of aspect ratio 5.0 with a 6% thick parabolic

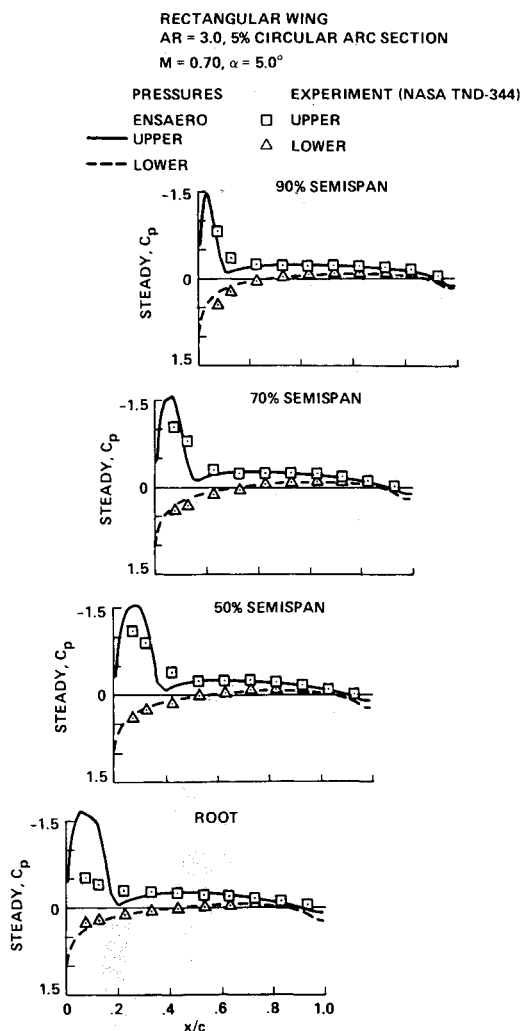


Fig. 6 Comparison of steady surface pressures between computation and experiment at $M = 0.70$ and $\alpha = 5.0$ deg.

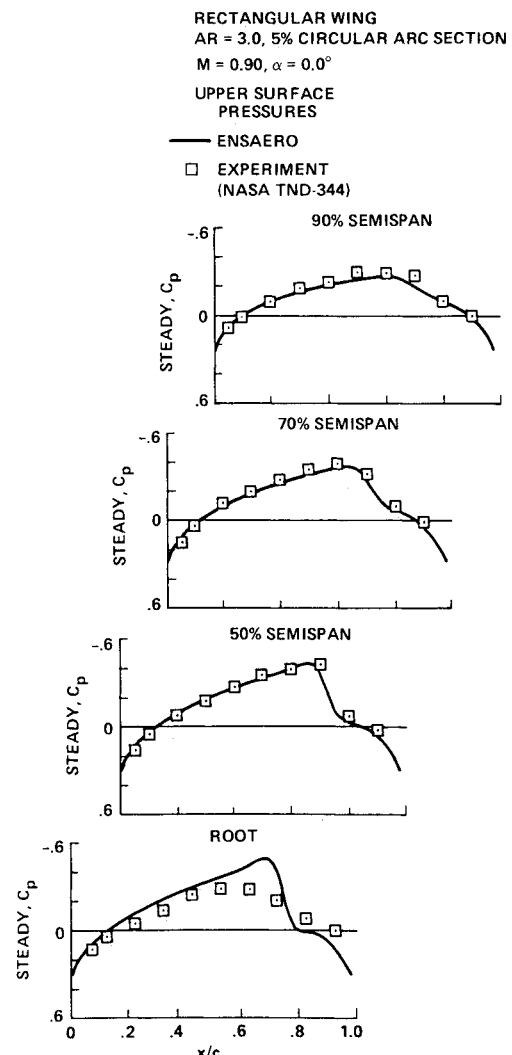


Fig. 7 Comparison of steady surface pressures between computation and experiment at $M = 0.90$ and $\alpha = 0.0$ deg.

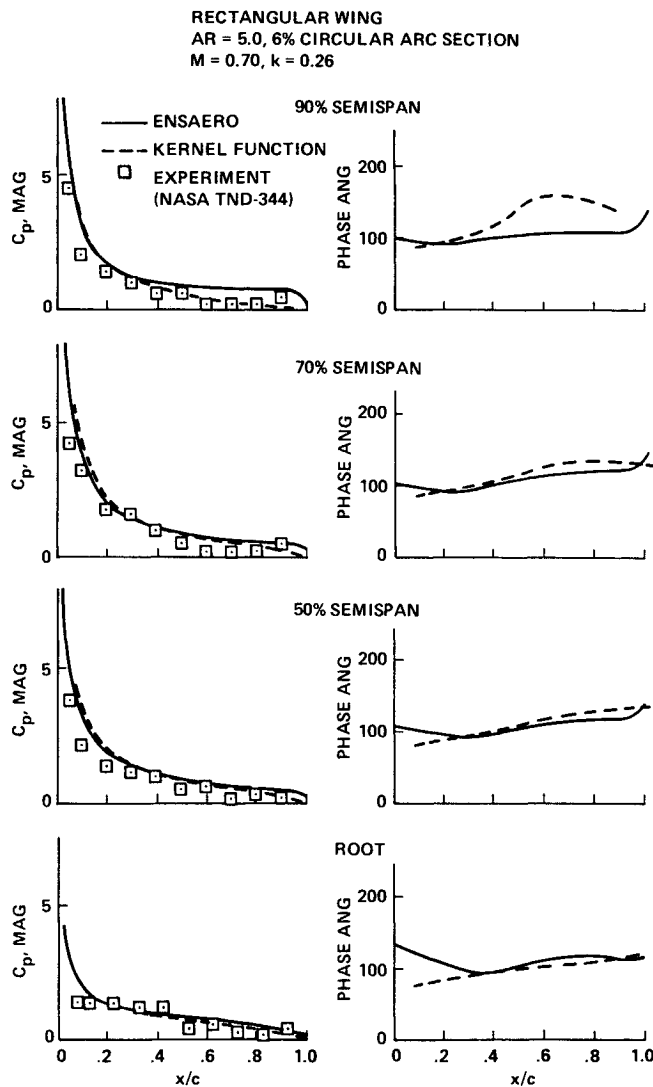


Fig. 8 Comparison of unsteady differential pressures between theories and experiment at $M = 0.70$ and $\alpha = 0.0$ deg.

air foil section. For this wing, flutter speeds at various flow conditions were measured in a wind tunnel and results are reported in Ref. 19. The length and the width of the model are 4.56 and 11.5 in., respectively.

Aeroelastic responses were computed by using the first five normal modes of the wing. The modal data required in the analysis were computed by modeling the wing with a 16-degree-of-freedom rectangular finite element.²⁰ Figure 10 shows the mode shapes and frequencies of the first five normal modes for the wing. This modal data compares well with the measured data.¹⁹ For example, the computed values of the natural frequencies of the first bending and torsional modes are 13.21 and 67.32 Hz, respectively. The corresponding measured values are 14.29 and 80.40 Hz, respectively. The computed values were obtained using the structural properties of the aluminum-alloy flat-plate insert in the model. The influence of the lightweight covering used for the wind-tunnel model to provide the thickness was not accounted for in the computations due to lack of available data. This might have caused the discrepancies between the computed and measured frequencies.

Using the normal modal data shown in Fig. 10, aeroelastic responses were computed by simultaneously integrating the flow equation [Eq. (5)] and the aeroelastic equation [Eq. (12)] in ENSAERO. The response calculations were started with initial modal disturbances in the first and second modes. To simulate these disturbances, the values for the first two generalized displacements, $q(1)$ and $q(2)$, were initially set to 0.2. The other values of $\{q\}$ were initially set to zero. Freestream

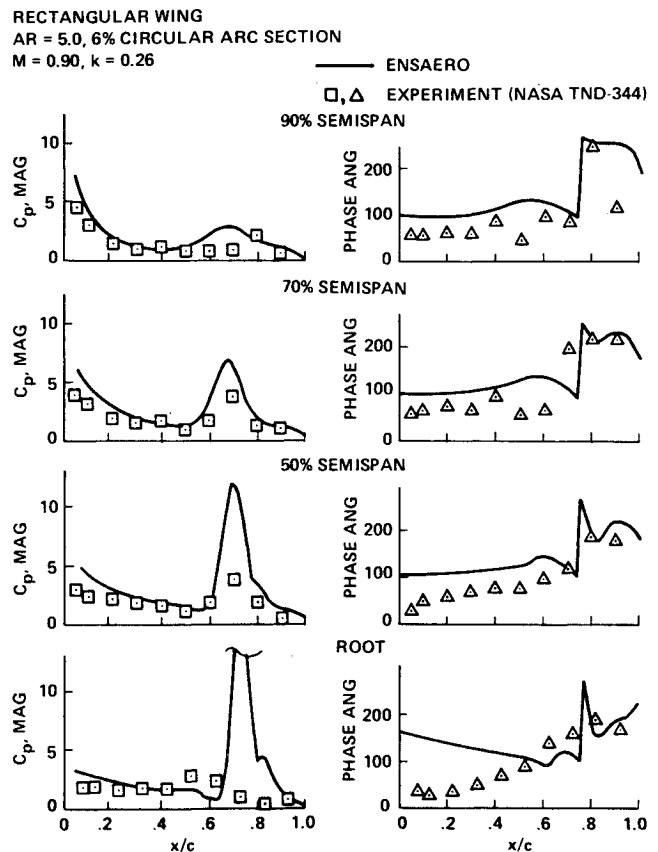


Fig. 9 Comparison of unsteady differential pressures between computed and experiment at $M = 0.90$ and $\alpha = 0.0$ deg.

conditions were used as initial conditions for the flow. An alternate method is to start from the converged steady-state solution. From numerical experiments of this work, it is found that numerical transients, those that are present at the start of the integration scheme, do not influence the aeroelastic responses. Identical solutions were obtained by both methods and all of the cases reported here are obtained using freestream conditions.

Aeroelastic responses were computed at $M = 0.715$ for various pressures. Figure 11 shows the stable, almost neutrally stable, and unstable responses of the first three coupled modes for dynamic pressures of 1.2, 1.4, and 1.6 psi, respectively. The response results are shown from the beginning of the computation. As observed from the results of the forced motions shown in the previous section, most of the numerical transients die out after the first cycle. Therefore, it was assumed for the results shown in Fig. 11 that the numerical transients die out after about 0.075 s, which corresponds to the physical time of completion of the first cycle of the first normal mode. The response of the first coupled mode in Fig. 11 is dominated by the first normal mode. The responses of the second and third coupled modes show predominantly the first normal mode superimposed with higher normal modes. After about 0.2 s the effect of the higher modes reduces.

The responses shown in Fig. 11 for the dynamic pressure of 1.4 psi are almost neutrally stable. It is noted that the experimental dynamic pressure measured at the neutrally stable condition for this case was 1.396 psi.¹⁹ The corresponding value obtained by using ATRAN3S,⁴ a code based on the transonic small-disturbance theory, is 1.56 psi. From this result, it can be stated that it is important to use the more exact equations such as the exact inviscid Euler equations to compute aeroelastic responses.

Computer Requirements

All of the preceding computations were made on the CRAY-XMP48 computer available at NASA Ames Research Center.

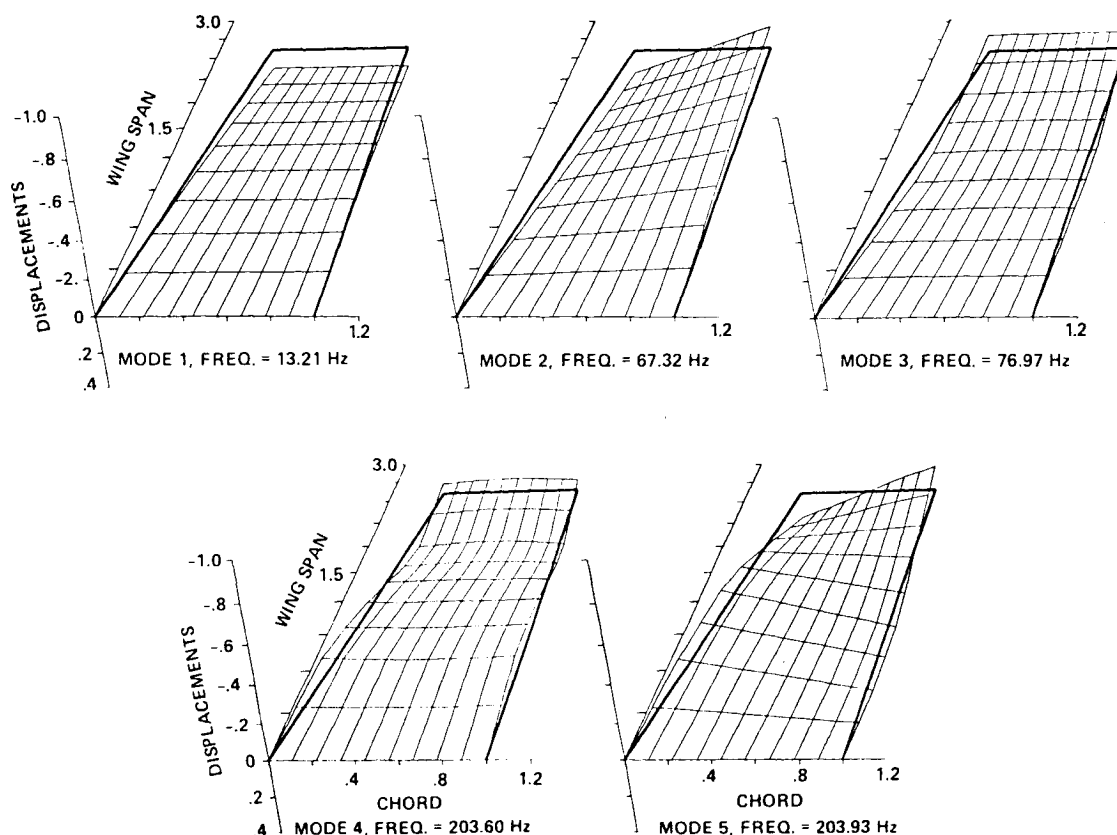


Fig. 10 Mode shapes and frequencies of the rectangular wing.

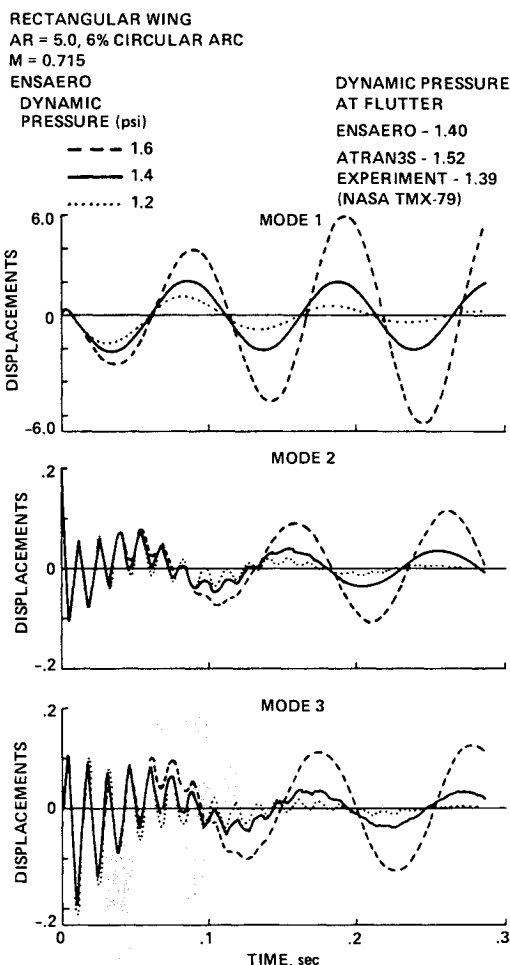


Fig. 11 Aeroelastic responses of the rectangular wing at $M = 0.715$ at three dynamic pressures.

For a grid size of $110 \times 20 \times 20$, the total memory required was 2.5 MW and CPU time per time step required was 1.5 s. Version 1.0 of ENSAERO runs at about 60 MFLOPS (million floating-point operations per second).

Conclusions

The following conclusions can be made based on the present work.

- 1) A time-accurate numerical procedure for computing the unsteady flows and aeroelastic responses of flexible wings using the Euler equations with configuration adaptive dynamic grids has been developed.
- 2) The unsteady results computed using dynamic grids compare well with the experiment.
- 3) Coupling of the Euler equations with the modal structural equations of motion is demonstrated for a rectangular wing.
- 4) The need for using more exact equations such as the exact inviscid Euler equations is demonstrated both for aerodynamic and aeroelastic computations.
- 5) Aeroelastic computations involving vortices need to be computed using finer grids in order to study possible aeroelastic instabilities due to these vortices.
- 6) This technique needs to be developed further using the Navier-Stokes equations for computing cases involving separated flows.

Appendix

Aerodynamic Solution Procedure

The basic Beam-Warming algorithm is first- or second-order accurate in time and second- or fourth-order accurate in space. The equations are factored (spatially split) which, for a given time iteration, reduces the process to three one-dimensional problems. Because of the second-order central-difference operators employed, the algorithm produces block tridiagonal systems for each spatial dimension. The stability and accuracy of the numerical algorithm is described by Beam and Warm-

ing.¹⁰ According to the linear analysis, the numerical scheme is unconditionally stable in two dimensions. In actual practice, time-step limits are encountered because of the nonlinear nature of the equations. However, this limitation is much less stringent than comparable explicit schemes. In three dimensions, the algorithm is unconditionally unstable, but stability is maintained by the addition of artificial dissipation terms.

The finite-difference algorithm of Beam and Warming applied to Eq. (5) results in the following approximate factorization:

$$\begin{aligned} & \left(I + h\delta_{\xi}\hat{A}^n + D_{\xi}^{(2)} \right) \left(I + h\delta_{\eta}\hat{B}^n + D_{\eta}^{(2)} \right) \\ & \times \left(I + h\delta_{\zeta}\hat{C}^n + D_{\zeta}^{(2)} \right) \Delta\hat{Q}^n = \hat{R}^n \\ & = -\Delta\tau \left(\delta_{\xi}\hat{E}^n + \delta_{\eta}\hat{F}^n + \delta_{\zeta}\hat{G}^n \right) - D^{(4)}\hat{Q}^n \end{aligned} \quad (A1)$$

where δ is the central-difference operator and Δ and ∇ are forward- and backward-difference operators. Indices denoting spatial location are suppressed, and $h = \Delta\tau$ corresponds to first-order time-accurate Euler implicit and $h = \Delta\tau/2$ to second-order time-accurate trapezoidal rules. The $D_{\xi}^{(2)}$, $D_{\eta}^{(2)}$, and $D_{\zeta}^{(2)}$ are the implicit smoothing operators and $D_e^{(4)}$ is the explicit smoothing operator.

The Jacobian matrices \hat{A}^n , \hat{B}^n , and \hat{C}^n are obtained by linearizing the flux vectors \hat{E}^n , \hat{F}^n , and \hat{G}^n in time such that

$$\hat{E}^{n+1} = \hat{E}^n + \hat{A}^n(\hat{Q}^{n+1} - \hat{Q}^n) + \mathcal{O}(\Delta\tau^2) \quad (A2a)$$

$$\hat{F}^{n+1} = \hat{F}^n + \hat{B}^n(\hat{Q}^{n+1} - \hat{Q}^n) + \mathcal{O}(\Delta\tau^2) \quad (A2b)$$

$$\hat{G}^{n+1} = \hat{G}^n + \hat{C}^n(\hat{Q}^{n+1} - \hat{Q}^n) + \mathcal{O}(\Delta\tau^2) \quad (A2c)$$

where indices denoting spatial location are suppressed again and

$$\hat{A} = \frac{\partial \hat{E}}{\partial \hat{Q}}, \quad \hat{B} = \frac{\partial \hat{F}}{\partial \hat{Q}}, \quad \hat{C} = \frac{\partial \hat{G}}{\partial \hat{Q}} \quad (A3)$$

are the flux Jacobian matrices.

Block tridiagonal-matrix inversions constitute the major portion of numerical work associated with the standard Beam-Warming algorithm. Equation (5) is a coupled set of five equations and thereby produces a (5×5) block-tridiagonal structure for the implicit operators of Eq. (A1). The diagonal version of the standard algorithm due to Pulliam and Chaussee¹³ overcomes this difficulty. In this algorithm, rather than inverting block-tridiagonal matrices in each direction, scalar pentadiagonal matrices are inverted. This is computationally more efficient.

The Jacobian matrices \hat{A} , \hat{B} , and \hat{C} have a set of eigenvalues and a complete set of distinct eigenvectors. Similarity transformations can be used to diagonalize \hat{A} , \hat{B} , and \hat{C} :

$$\hat{A} = T_{\xi}\hat{\Lambda}_{\xi}T_{\xi}^{-1}, \quad \hat{B} = T_{\eta}\hat{\Lambda}_{\eta}T_{\eta}^{-1}, \quad \hat{C} = T_{\zeta}\hat{\Lambda}_{\zeta}T_{\zeta}^{-1} \quad (A4)$$

where

$$\hat{\Lambda}_{\xi} = D \begin{bmatrix} U, U, U, U + c(\xi_x^2 + \xi_y^2 + \xi_z^2)^{1/2}, \\ U - c(\xi_x^2 + \xi_y^2 + \xi_z^2)^{1/2} \end{bmatrix} \quad (A5a)$$

$$\hat{\Lambda}_{\eta} = D \begin{bmatrix} V, V, V, V + c(\eta_x^2 + \eta_y^2 + \eta_z^2)^{1/2}, \\ V - c(\eta_x^2 + \eta_y^2 + \eta_z^2)^{1/2} \end{bmatrix} \quad (A5b)$$

$$\hat{\Lambda}_{\zeta} = D \begin{bmatrix} W, W, W, W + c(\zeta_x^2 + \zeta_y^2 + \zeta_z^2)^{1/2}, \\ W - c(\zeta_x^2 + \zeta_y^2 + \zeta_z^2)^{1/2} \end{bmatrix} \quad (A5c)$$

where c is the speed of sound ($c^2 = \gamma p / \rho$).

The similarity transformation matrices T_{ξ} , T_{η} , and T_{ζ} and their inverse matrices are given in Ref. 13. Relations exist

between T_{ξ} , T_{η} , and T_{ζ} of the form

$$\begin{aligned} \hat{N} &= T_{\xi}^{-1}T_{\eta}, \quad \hat{N}^{-1} = T_{\eta}^{-1}T_{\xi}, \quad \hat{P} = T_{\eta}^{-1}T_{\zeta} \\ \hat{P}^{-1} &= T_{\zeta}^{-1}T_{\eta} \end{aligned} \quad (A6)$$

After applying the similarity transformations of Eqs. (A4) and identities of Eq. (A6), and exchanging the smoothing operators with new ones, the diagonal form of the standard algorithm reads

$$\begin{aligned} & T_{\xi}(I + h\delta_{\xi}\hat{\Lambda}_{\xi} - hD_i|_{\xi})\hat{N}(I + h\delta_{\eta}\hat{\Lambda}_{\eta} - hD_i|_{\eta}) \\ & \times \hat{P}(I + h\delta_{\zeta}\hat{\Lambda}_{\zeta} - hD_i|_{\zeta})T_{\zeta}^{-1}\Delta\hat{Q}^n = \hat{R}^n \end{aligned} \quad (A7)$$

This diagonal scheme reduces the Beam-Warming scheme to, at most, first-order in time and also gives time-accurate shock calculations in a nonconservative mode.

References

- Kutler, P., Steger, J. L., and Bailey, F. R., "Status of Computational Fluid Dynamics in United States," AIAA Paper 87-1135, June 1987.
- Holst, T., "Numerical Solution of the Navier-Stokes Equations about Three-Dimensional Configurations—A Survey," NASA CP-2454, March 1987.
- Flores, J., "Simulation of Transonic Viscous Wing and Wing-Fuselage Flows Using Zonal Methods," NASA TM 89421, March 1987.
- Guruswamy, G. P. and Tu, E. L., "Effects of Symmetric and Asymmetric Modes on Transonic Aeroelastic Characteristics of Full-Span Wing-Body Configuration," AIAA Paper 88-2308, April 1988.
- Guruswamy, G. P., Goorjian, P. M., Ide, H., and Miller, G. D., "Transonic Aeroelastic Analysis of the B-1 Wing," *Journal of Aircraft*, Vol. 23, July 1986, pp. 547-553.
- Dobbs, S. K. and Miller, G. D., "Self-Induced Oscillation Wind-Tunnel Test of a Variable Sweep Wing," AIAA Paper 85-0739, April 1985.
- Borland, C. J. and Rizzetta, D. P., "Transonic Unsteady Aerodynamics for Aeroelastic Applications, Vol. I—Technical Development Summary," Air Force Wright Aeronautical Laboratories, AFWAL TR-80-3107, June 1980.
- Peterson, V. L. and Ballhaus, W. F., "History of the Numerical Aerodynamic Simulation Program," NASA CP-2454, March 1987.
- Pulliam, T. H. and Steger, J. L., "Implicit Finite-Difference Simulations of Three-Dimensional Compressible Flow," *AIAA Journal*, Vol. 18, Feb. 1980, pp. 159-167.
- Beam, R. and Warming, R. F., "An Implicit Finite-Difference Algorithm for Hyperbolic Systems in Conservation Law Form," *Journal of Computational Physics*, Vol. 22, Sept. 1976, pp. 87-110.
- Ying, S. X., Steger, J. L., and Schiff, L. B., "Numerical Simulation of Unsteady, Viscous, High Angle-of-Attack Flows Using a Partial Flux Split Algorithm," AIAA Paper 86-2179, Aug. 1986.
- Goorjian, P. M., "A New Algorithm for the Navier-Stokes Equations Applied to Transonic Flows Over Wings," AIAA Paper 87-1121-CP, June 1987.
- Pulliam, T. H. and Chaussee, D. S., "A Diagonal Form of an Implicit Approximate Factorization Algorithm," *Journal of Computational Physics*, Vol. 39, Feb. 1981, pp. 347-363.
- Peyret, R. and Viviani, H., "Computation of Viscous Compressible Flows Based on Navier-Stokes Equations," AGARD-AG-212, 1975.
- Guruswamy, P. and Yang, T. Y., "Aeroelastic Time-Response Analysis of Thin Airfoils by Transonic Code LTRAN2," *Computers and Fluids*, Vol. 9, No. 4, Dec. 1980, pp. 409-425.
- Davis, S. S. and Malcolm, G. N., "Experimental Unsteady Aerodynamics of Conventional and Supercritical Airfoils," NASA TM 81221, Aug. 1980.
- Guruswamy, G. P. and Goorjian, P. M., "Effects of Viscosity on Transonic-Aerodynamic and Aeroelastic Characteristics of Oscillating Airfoils," *Journal of Aircraft*, Vol. 21, Sept. 1984, pp. 700-707.
- Lessing, H. C., Troutman, J. L., and Menees, G. P., "Experimental Determination of the Pressure Distribution on a Rectangular Wing Oscillating in First Bending Mode for Mach Numbers from 0.24-1.30," NASA TN D-344, Dec. 1960.
- Doggett, R. V., Rainey, A. G., and Morgan, H. G., "An Experimental Investigation of Aerodynamic Effects of Airfoil Thickness on Transonic Flutter Characteristics," NASA TMX-79, 1959.
- Guruswamy, G. P., "Special-Purpose Finite-Element Programs," *Finite-Element Structural Analysis*, edited by T. Y. Yang, Prentice Hall, New York, 1986, Chap. 13.